Journal of the Brazilian Society of Mechanical Sciences and Engineering (2019) 41:149
https://doi.org/10.1007/s40430-019-1647-5

TECHNICAL PAPER

Axisymmetric flow by a rotating disk with Cattaneo–Christov heat flux

Maria Imtiaz[1] · Asmara Kiran[2] · Tasawar Hayat[2,3] · Ahmed Alsaedi[3]

Received: 23 May 2018 / Accepted: 13 February 2019 / Published online: 27 February 2019

Abstract

Here, axisymmetric flow of Jeffrey fluid by a rotating disk with variable thicked surface is studied. Heat transfer is discussed through Cattaneo–Christov heat flux model. Transformation procedure has been adopted in obtaining ordinary differential systems. Convergent series solutions are obtained. Flow, temperature and skin friction coefficient for various parameters of interest are graphically illustrated. The radial and tangential velocities are increasing functions of Deborah number.

Keywords Variable thickness · Jeffrey fluid · Rotating disk · Cattaneo–Christov heat flux

1 Introduction

Non-Newtonian fluid has significant applications in industrial and technological processes. It plays a great role in food processing, suspensions, certain oils, lubrications, nourishment preparing, polymer, biomechanics, manufacturing of paints and emulsions, etc. Non-Newtonian fluids are much complex because of additional rheological parameters in constitutive relationship. Materials like soap solutions, ketchup, blood, apple sauce are common examples of non-Newtonian fluids. Classifications of non-Newtonian fluids are through integral, rate and differential types. Jeffrey fluid describes the phenomenon of relaxation and retardation times. Narayana and Babu [1] investigated stretched flow of Jeffrey fluid with magnetohydrodynamics and thermal radiation. Turkyilmazoglu [2] described magnetic field and slip effects on the flow and heat transfer of stagnation point Jeffrey fluid over deformable surfaces. Abbasi et al. [3] presented convective flow of Jeffrey fluid in the presence of thermal radiation and magnetohydrodynamics (MHD). Shehzad et al. [4] scrutinized MHD radiative flow of Jeffrey fluid. Heat transfer in MHD flow of Jeffrey fluid over a stretching sheet is inspected by Zeeshan and Majeed [5]. Dalir [6] focused on stretched flow of Jeffrey fluid with entropy generation. Turkyilmazoglu and Pop [7] analyzed stagnation point flow of Jeffrey fluid. Hayat et al. [8] described three-dimensional flow of Jeffrey fluid due to a stretching surface.

Flow due to rotating surfaces has promising applications in engineering and industrial sectors such as lubrication, air cleaning machine, electric power generating system, turbo machinery, gas turbine, food processing technology and centrifugal machinery. Flow due to rotating disk is initially studied by Karman [9]. He provided von Karman transformations to convert Navier–Stokes equations into ordinary differential equations. Ming et al. [10] worked on steady flow and heat transfer of the power law fluid over a rotating disk. Rotating flow of nanofluid with heat transfer is illustrated by Turkyilmazoglu [11]. Bayat et al. [12] investigated magneto-thermo-mechanical response in a functionally graded annular over a rotating disk. Sheikholeslami et al. [13] analyzed nanofluid flow due to a rotating disk. Rotating flow of Jeffrey fluid with magnetohydrodynamics is done by Hayat et al. [14]. Turkyilmazoglu [15] studied flow and heat transfer due to a rotating disk. Hayat et al. [16] presented influence of Cattaneo–Christov heat flux in flow of Jeffrey fluid due to a rotating disk. Saidi and Tamim [17] examined unsteady flow of nanofluid between two rotating disks. Flow of Ostwald–de Waele fluid with

Technical Editor: Jader Barbosa Jr., Ph.D.

✉ Maria Imtiaz
mi_qau@yahoo.com

[1] Department of Mathematics, University of Wah, Wah Cantt 47040, Pakistan

[2] Department of Mathematics, Quaid-I-Azam University 45320, Islamabad 44000, Pakistan

[3] Nonlinear Analysis and Applied Mathematics (NAAM) Research Group, Department of Mathematics, Faculty of Science, King Abdulaziz University, Jeddah 21589, Saudi Arabia

heat transfer analysis by a rotating disk is studied by Xun et al. [18].

The phenomenon of heat transfer has numerous applications in industry and engineering processes, e.g., nuclear reactor cooling, energy production, cooling of electronic devices, transportations, micro electronics and fuel cells, etc. Heat transfer phenomenon was successfully presented by Fourier heat conduction law [19]. This model has some limitations that whole medium is sensed instantly by the initial disturbance (main drawback of this model). This unrealistic argument is named as “paradox of heat conduction”. In order to resolve this problem, Cattaneo [20] proposed Fourier law of heat conduction by adding a thermal relaxation time. Christov [21] further worked on Cattaneo’s model by introducing Oldroyd upper convectived derivative. Impact of Cattaneo–Christov heat flux model in the flow of viscoelastic fluid is illustrated by Tibullo and Zampoli [22]. Han et al. [23] described flow of viscoelastic fluid in the existence of Cattaneo–Christov heat flux model. Hayat et al. [24] examined effects of magnetohydrodynamic in the flow of Oldroyd-B fluid with Cattaneo–Christov heat flux model. Analysis of heat transfer through Cattaneo–Christov heat flux model in nanofluid flow by a stretched surface is studied by Sui et al. [25]. Mustafa [26] discussed rotating flow of Maxwell fluid in the presence of Cattaneo–Christov heat flux model. Li et al. [27] presented influence of Cattaneo–Christov heat flux model in viscoelastic fluid flow due to a stretching sheet.

Present analysis examines the axisymmetric three-dimensional flow of Jeffrey fluid due to a rotating disk with variable thickness. Heat transfer analysis is examined by Cattaneo–Christov heat flux. Solution expressions of nonlinear problem are obtained by homotopy analysis method [28–35]. Influence of various involved parameters on axial, radial and tangential velocities, temperature and surface drag force is discussed graphically.

2 Model development

Here, we have an interest to examine flow of Jeffrey fluid by a disk with variable thickness. Disk rotates with constant angular velocity Ω. Temperatures at disk and away from it are denoted by T_w and T_∞ (see Fig. 1). The resulting equations for flow and thermal fields [18] are

$$\frac{\partial u}{\partial r}+\frac{u}{r}+\frac{\partial w}{\partial z}=0, \tag{1}$$

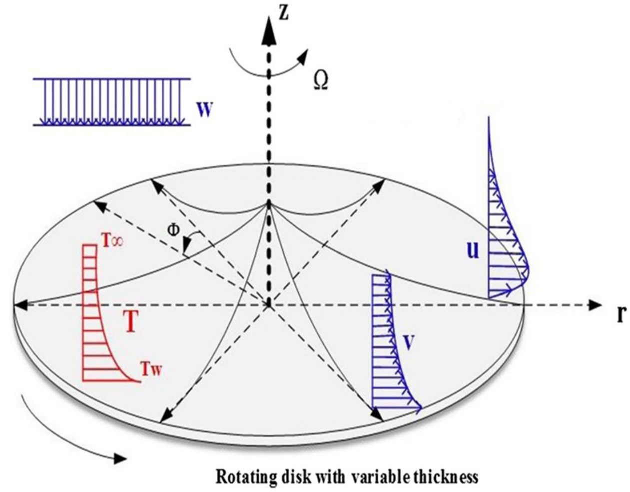

Fig. 1 Flow geometry

$$\left(u\frac{\partial u}{\partial r}+w\frac{\partial u}{\partial z}-\frac{v^2}{r}\right)=\frac{\nu}{1+\lambda_1}\frac{\partial^2 u}{\partial z^2}+\frac{\lambda_2\nu}{1+\lambda_1}\left(2u\frac{\partial^3 u}{\partial r\partial z^2}+2w\frac{\partial^3 u}{\partial z^3}+\frac{\partial u}{\partial z}\frac{\partial^2 u}{\partial r\partial z}+\frac{\partial w}{\partial z}\frac{\partial^2 u}{\partial z^2}\right), \tag{2}$$

$$\left(u\frac{\partial v}{\partial r}+w\frac{\partial v}{\partial z}+\frac{uv}{r}\right)=\frac{\nu}{1+\lambda_1}\frac{\partial^2 v}{\partial z^2}+\frac{\lambda_2\nu}{1+\lambda_1}\left(2u\frac{\partial^3 v}{\partial r\partial z^2}+2w\frac{\partial^3 v}{\partial z^3}+\frac{\partial u}{\partial z}\frac{\partial^2 v}{\partial r\partial z}+\frac{\partial w}{\partial z}\frac{\partial^2 v}{\partial z^2}\right), \tag{3}$$

$$\rho C_p\left(u\frac{\partial T}{\partial r}+w\frac{\partial T}{\partial z}\right)=-\nabla.\mathbf{q}, \tag{4}$$

with

$$u=0,\ \mathrm{v}=\Omega r, w=0, T=T_w \ \text{ at } z=a\left(\frac{r}{R_0}+1\right)^{-m}, \quad u=0,\ \mathrm{v}=0,\ T=T_\infty \ \text{ when } z\to\infty, \tag{5}$$

where $u(r,\theta,z)$, $\mathrm{v}(r,\theta,z)$ and $w(r,\theta,z)$ are components of velocity $\mathbf{V}$, ν denotes the kinematic viscosity, μ the dynamic viscosity, ρ the density of fluid, m the disk thickness index, R_0 the dimensional constant, C_p the specific heat, a the thickness coefficient of disk, λ_1 the ratio of relaxation to retardation times and λ_2 the retardation time. Here, heat flux $\mathbf{q}$ obeys

$$\mathbf{q}+\lambda\left(\frac{\partial\mathbf{q}}{\partial t}+\mathbf{V}.\nabla\mathbf{q}-\mathbf{q}.\nabla\mathbf{V}+(\nabla.\mathbf{V})\mathbf{q}\right)=-k\nabla T, \tag{6}$$

in which k and λ elucidate the thermal conductivity and relaxation time. Incompressible situation leads to

$$\mathbf{q}+\lambda\left(\frac{\partial \mathbf{q}}{\partial t}+\mathbf{V}.\nabla\mathbf{q}-\mathbf{q}.\nabla\mathbf{V}\right)=-k\nabla T, \tag{7}$$

Expressions (4) and (7) give

$$u\frac{\partial T}{\partial r}+w\frac{\partial T}{\partial z}=\frac{k}{\rho C_p}\frac{\partial^2 T}{\partial z^2}-\lambda\left[u^2\frac{\partial^2 T}{\partial r^2}+w^2\frac{\partial^2 T}{\partial z^2}+2uw\frac{\partial^2 T}{\partial r\partial z}+\left(u\frac{\partial u}{\partial r}+w\frac{\partial u}{\partial z}\right)\frac{\partial T}{\partial r}+\left(u\frac{\partial w}{\partial r}+w\frac{\partial w}{\partial z}\right)\frac{\partial T}{\partial z}\right]. \tag{8}$$

Following transformations

$$u=r\Omega F(\eta),\ \mathrm{v}=r\Omega G(\eta), w=-R_0\Omega\left(1+\frac{r}{R_0}\right)^{-m}\left(\frac{\Omega R_0^2\rho}{\mu}\right)^{-\frac{1}{n+1}}J(\eta),$$
$$\eta=\frac{z}{R_0}\left(\frac{\Omega R_0^2\rho}{\mu}\right)^{\frac{1}{n+1}}\left(1+\frac{r}{R_0}\right)^{m},\Theta=\frac{T-T_\infty}{T_w-T_\infty}. \tag{9}$$

Using Eq. (9), Eqs. (1–3) and (8) become

$$J'+2F+m\eta\epsilon F'=0, \tag{10}$$

$$\mathrm{Re}^{\frac{1-n}{1+n}}(1+r^*)^{2m}F''+\beta\mathrm{Re}^{\frac{1-n}{1+n}}(1+r^*)^{2m}\big(2FF''+4m\epsilon FF''+2m\epsilon\eta FF'''-2JF'''+F'^2+\epsilon F'^2+m\eta\epsilon F'F''-J'F''\big)-(1+\lambda_1)(F^2-G^2+JF'+m\eta\epsilon FF')=0, \tag{11}$$

$$\mathrm{Re}^{\frac{1-n}{1+n}}(1+r^*)^{2m}G''+\beta\mathrm{Re}^{\frac{1-n}{1+n}}(1+r^*)^{2m}\big(2FG''+4m\epsilon FG''+2m\epsilon\eta FG'''-2JG'''+F'G'+m\epsilon F'G'+m\eta\epsilon F'G''-J'G''\big)-(1+\lambda_1)(2FG+JG'+m\eta\epsilon FG')=0, \tag{12}$$

$$\frac{1}{\mathrm{Pr}}\mathrm{Re}^{\frac{1-n}{1+n}}(1+r^*)^{2m}\Theta''-\gamma\big(m(m-1)\eta\epsilon^2F^2\Theta''+J^2\Theta''+m\epsilon JF\Theta'+m\eta\epsilon F^2\Theta'+m^2\eta^2\epsilon^2FF'\Theta'+m\eta\epsilon JF'\Theta'+m\eta r^*FJ'\Theta'+JJ'\Theta\big)-m\eta\epsilon F\Theta'-J\Theta'=0, \tag{13}$$

$$F(\alpha)=0, G(\alpha)=1, J(\alpha)=0, \Theta(\alpha)=1,\quad F(\infty)=0, G(\infty)=0, \Theta(\infty)=0. \tag{14}$$

Letting

$$j(\xi)=j(\eta-\alpha)=J(\eta), f(\xi)=f(\eta-\alpha)=F(\eta),\quad g(\xi)=g(\eta-\alpha)=G(\eta), \theta(\xi)=\theta(\eta-\alpha)=\Theta(\eta), \tag{15}$$

we have

$$j'+2f+m(\xi+\alpha)\epsilon f'=0, \tag{16}$$

$$\mathrm{Re}^{\frac{1-n}{1+n}}(1+r^*)^{2m}f''+\beta\mathrm{Re}^{\frac{1-n}{1+n}}(1+r^*)^{2m}\big(2ff''+4m\epsilon ff''+2m\epsilon(\xi+\alpha)ff'''-2jf'''+f'^2+\epsilon f'^2+m(\xi+\alpha)\epsilon f'f''-j'f''\big)-(1+\lambda_1)(f^2-g^2+jf'+m(\xi+\alpha)\epsilon ff')=0, \tag{17}$$

$$\mathrm{Re}^{\frac{1-n}{1+n}}(1+r^*)^{2m}g''+\beta\mathrm{Re}^{\frac{1-n}{1+n}}(1+r^*)^{2m}\big(2fg''+4m\epsilon fg''+2m\epsilon(\xi+\alpha)fg'''-2jg'''+f'g'+m\epsilon f'g'+m(\xi+\alpha)\epsilon f'g''-j'g''\big)-(1+\lambda_1)(2fg+jg'+m(\xi+\alpha)\epsilon fg')=0, \tag{18}$$

$$\frac{1}{\mathrm{Pr}}\mathrm{Re}^{\frac{1-n}{1+n}}(1+r^*)^{2m}\theta''-\gamma\big(m(m-1)(\xi+\alpha)\epsilon^2f^2\theta''+j^2\theta''+m\epsilon jf\theta'+m(\xi+\alpha)\epsilon f^2\theta'+m^2(\xi+\alpha)^2\epsilon^2ff'\theta'+m(\xi+\alpha)\epsilon jf'\theta'+m(\xi+\alpha)r^*fj'\theta'+jj'\theta\big)-m(\xi+\alpha)\epsilon f\theta'-j\theta'=0, \tag{19}$$

$$f(0)=0, g(0)=1, j(0)=0, \theta(0)=1,\quad f(\infty)=0, g(\infty)=0, \theta(\infty)=0, \tag{20}$$

with

$$\mathrm{Re}=\frac{\Omega R_0^2\rho}{\mu}, \alpha=\frac{a}{R_0}\left(\frac{\Omega R_0^2\rho}{\mu}\right)^{\frac{1}{n+1}}, \epsilon=\frac{r}{R_0+r},\quad r^*=\frac{r}{R_0}, \mathrm{Pr}=\frac{c_p\mu}{k}, \gamma=\lambda\Omega, \beta=\lambda_2\Omega. \tag{21}$$

Here, Re depicts the Reynolds number, α the dimensionless coefficient of disk, ϵ the dimensionless constant, r^* the radius parameter, Pr the Prandtl number, γ the nondimensional thermal relaxation parameter, β the Deborah number and n the power law exponent of fluid. Also, (f, g, j and θ) are dimensionless (radial, tangential and axial) velocities and temperature.

Skin friction coefficient in radial and axial directions are

$$C_{f_r}=\tau_{wr}/\rho(\Omega R_0)^2,\quad C_{f_\theta}=\tau_{w\theta}/\rho(\Omega R_0)^2, \tag{22}$$

in which radial shear stress (τ_{wr}) and tangential shear stress ($\tau_{w\theta}$) satisfy

$$\tau_{w\theta}=\frac{\mu}{1+\lambda_1}\left[\frac{\partial v}{\partial z}+\lambda_2\left(u\frac{\partial}{\partial r}+w\frac{\partial}{\partial z}\right)\frac{\partial v}{\partial z}\right]\Big|_{z=a\left(\frac{r}{R_0}+1\right)^{-m}}. \tag{23}$$

Radial and tangential skin friction coefficients are

$$\mathrm{Re}^{\frac{n}{n+1}}C_{f_r}=\frac{(1+r^*)^m}{r^*(1+\lambda_1)}\big[f'(0)+\beta(f(0)f'(0)+m\epsilon f(0)f'(0)+m\eta\epsilon f(0)f''(0)-h(0)f''(0))\big],$$
$$\mathrm{Re}^{\frac{n}{n+1}}C_{f_\theta}=\frac{(1+r^*)^m}{r^*(1+\lambda_1)}\big[g'(0)+\beta(f(0)g'(0)+m\epsilon f(0)g'(0)+m\eta\epsilon h(0)g''(0)-h(0)g''(0))\big]. \tag{24}$$

3 Solutions procedure

Initial guesses $j_0(\xi), f_0(\xi), g_0(\xi)$ and $\theta_0(\xi)$ are

$$j_0(\xi)=0, f_0(\xi)=0, g_0(\xi)=e^{-\xi}, \theta_0(\eta)=e^{-\xi}, \tag{25}$$

where linear operators $\mathcal{L}_j, \mathcal{L}_f, \mathcal{L}_g$ and $\mathcal{L}_\theta$ are

$$\mathcal{L}_j=j', \mathcal{L}_f=f''-f, \mathcal{L}_g=g''-g, \mathcal{L}_\theta=\theta''-\theta. \tag{26}$$

with

$$\begin{aligned}\mathcal{L}_j[c_1]&=0,\\ \mathcal{L}_f\left[c_2e^{\xi}+c_3e^{-\xi}\right]&=0,\\ \mathcal{L}_g[c_4e^{\xi}+c_5e^{-\xi}]&=0,\\ \mathcal{L}_\theta\left[c_6e^{\xi}+c_7e^{-\xi}\right]&=0,\end{aligned} \tag{27}$$

in which $c_i\,(i=1-7)$ denote the constants.

3.1 Zeroth-order deformation problems

Considering $p\in[0,1]$ as embedding and ($\hbar_j, \hbar_f, \hbar_g$ and $\hbar_\theta$) the nonzero auxiliary parameters, then zeroth-order deformation problems are

$$(1-p)\mathcal{L}_j\left[\hat{j}(\xi,p)-j_0(\xi)\right]=p\hbar_j\mathcal{N}_j[\hat{j}(\xi,p),\hat{f}(\xi,p)], \tag{28}$$

$$(1-p)\mathcal{L}_f\left[\hat{f}(\xi,p)-f_0(\xi)\right]=p\hbar_f\mathcal{N}_f[\hat{f}(\xi,p),\hat{g}(\xi,p)], \tag{29}$$

$$(1-p)\mathcal{L}_g\left[\hat{g}(\xi,p)-g_0(\xi)\right]=p\hbar_g\mathcal{N}_g[\hat{f}(\xi,p),\hat{g}(\xi,p)], \tag{30}$$

$$(1-p)\mathcal{L}_\theta\left[\hat{\theta}(\xi,p)-\theta_0(\xi)\right]=p\hbar_\theta\mathcal{N}_\theta[\hat{\theta}(\xi,p),\hat{f}(\xi,p),\hat{j}(\xi,p)], \tag{31}$$

$$\mathcal{N}_j\left[\hat{j}(\xi,p),\hat{f}(\xi,p)\right]=\frac{\partial\hat{j}(\xi,p)}{\partial\xi}+2\hat{f}(\xi,p)+m(\xi+\alpha)\epsilon\frac{\partial\hat{f}(\xi,p)}{\partial\xi}, \tag{32}$$

$$\begin{aligned}&\mathcal{N}_f\left[\hat{f}(\xi,p),\hat{g}(\xi,p)\right]=\mathrm{Re}^{\frac{1-n}{1+n}}(1+r^*)^{2m}\frac{\partial^2\hat{f}(\xi,p)}{\partial\xi^2}\\&+\beta\mathrm{Re}^{\frac{1-n}{1+n}}(1+r^*)^{2m}\Bigg(2\hat{f}(\xi,p)\frac{\partial^2\hat{f}(\xi,p)}{\partial\xi^2}\\&+4m\epsilon\hat{f}(\xi,p)\frac{\partial^2\hat{f}(\xi,p)}{\partial\xi^2}+2m\epsilon(\xi+\alpha)\hat{f}(\xi,p)\frac{\partial^3\hat{f}(\xi,p)}{\partial\xi^3}\\&-2\hat{j}(\xi,p)\frac{\partial^3\hat{f}(\xi,p)}{\partial\xi^3}\\&+\left(\frac{\partial\hat{f}(\xi,p)}{\partial\xi}\right)^2+\epsilon\left(\frac{\partial\hat{f}(\xi,p)}{\partial\xi}\right)^2+m(\xi+\alpha)\epsilon\frac{\partial\hat{f}(\xi,p)}{\partial\xi}\frac{\partial^2\hat{f}(\xi,p)}{\partial\xi^2}\\&-\frac{\partial\hat{j}(\xi,p)}{\partial\xi}\frac{\partial^2\hat{f}(\xi,p)}{\partial\xi^2}\Bigg)-(1+\lambda_1)\left(\left(\frac{\partial\hat{f}(\xi,p)}{\partial\xi}\right)^2-\left(\frac{\partial\hat{g}(\xi,p)}{\partial\xi}\right)^2\right.\\&\left.+\hat{j}(\xi,p)\frac{\partial\hat{f}(\xi,p)}{\partial\xi}+m(\xi+\alpha)\epsilon\hat{f}(\xi,p)\frac{\partial\hat{f}(\xi,p)}{\partial\xi}\right),\end{aligned} \tag{33}$$

$$\begin{aligned}&\mathcal{N}_g\left[\hat{f}(\xi,p),\hat{g}(\xi,p)\right]=\mathrm{Re}^{\frac{1-n}{1+n}}(1+r^*)^{2m}\frac{\partial^2\hat{g}(\xi,p)}{\partial\xi^2}\\&+\beta\mathrm{Re}^{\frac{1-n}{1+n}}(1+r^*)^{2m}\Bigg(2\hat{f}(\xi,p)\frac{\partial^2\hat{g}(\xi,p)}{\partial\xi^2}\\&+4m\epsilon\hat{f}(\xi,p)\frac{\partial^2\hat{g}(\xi,p)}{\partial\xi^2}+2m\epsilon(\xi+\alpha)\hat{f}(\xi,p)\frac{\partial^3\hat{g}(\xi,p)}{\partial\xi^3}\\&-2\hat{j}(\xi,p)\frac{\partial^3\hat{g}(\xi,p)}{\partial\xi^3}\\&+\frac{\partial\hat{f}(\xi,p)}{\partial\xi}\frac{\partial\hat{g}(\xi,p)}{\partial\xi}+\epsilon\frac{\partial\hat{f}(\xi,p)}{\partial\xi}\frac{\partial\hat{g}(\xi,p)}{\partial\xi}+m(\xi+\alpha)\epsilon\frac{\partial\hat{f}(\xi,p)}{\partial\xi}\frac{\partial^2\hat{g}(\xi,p)}{\partial\xi^2}\\&-\frac{\partial\hat{j}(\xi,p)}{\partial\xi}\frac{\partial^2\hat{g}(\xi,p)}{\partial\xi^2}\Bigg)-(1+\lambda_1)\Bigg(2\hat{f}(\xi,p)\hat{g}(\xi,p)+\hat{j}(\xi,p)\frac{\partial\hat{g}(\xi,p)}{\partial\xi}\\&+m(\xi+\alpha)\epsilon\hat{f}(\xi,q)\frac{\partial\hat{g}(\xi,p)}{\partial\xi}\Bigg),\end{aligned} \tag{34}$$

$$\begin{aligned}&\mathcal{N}_\theta\left[\hat{\theta}(\xi,p),\hat{f}(\xi,p),\hat{j}(\xi,p)\right]=\frac{1}{\mathrm{Pr}}\mathrm{Re}^{\frac{1-n}{1+n}}(1+r^*)^{2m}\frac{\partial^2\hat{\theta}(\xi,p)}{\partial\xi^2}\\&-\gamma\Bigg(m(m-1)(\xi+\alpha)\epsilon^2\left(\hat{f}(\xi,q)\right)^2\frac{\partial^2\hat{\theta}(\xi,p)}{\partial\xi^2}\\&+(\hat{j}(\xi,p))^2\frac{\partial^2\hat{\theta}(\xi,p)}{\partial\xi^2}+m\epsilon\hat{j}(\xi,p)\hat{f}(\xi,p)\frac{\partial\hat{\theta}(\xi,p)}{\partial\xi}+m(\xi+\alpha)\epsilon\left(\hat{f}(\xi,q)\right)^2\\&\quad\frac{\partial\hat{\theta}(\xi,p)}{\partial\xi}+m^2(\xi+\alpha)\epsilon^2\hat{f}(\xi,q)\frac{\partial\hat{f}(\xi,p)}{\partial\xi}\frac{\partial\hat{\theta}(\xi,p)}{\partial\xi}+m(\xi+\alpha)\epsilon\hat{j}(\xi,p)\frac{\partial\hat{f}(\xi,p)}{\partial\xi}\\&\quad\frac{\partial\hat{\theta}(\xi,p)}{\partial\xi}+m(\xi+\alpha)r^*\hat{f}(\xi,q)\frac{\partial\hat{j}(\xi,p)}{\partial\xi}\frac{\partial\hat{\theta}(\xi,p)}{\partial\xi}+\hat{j}(\xi,p)\frac{\partial\hat{j}(\xi,p)}{\partial\xi}\hat{\theta}(\xi,p)\Bigg)\\&-m(\xi+\alpha)\epsilon\hat{f}(\xi,q)\frac{\partial\hat{\theta}(\xi,p)}{\partial\xi}-\hat{j}(\xi,p)\frac{\partial\hat{\theta}(\xi,p)}{\partial\xi},\end{aligned} \tag{35}$$

$$\begin{aligned}&\hat{j}(0,p)=0, \hat{f}(0,p)=0, \hat{g}(0,p)=1, \hat{\theta}(0,p)=1,\\&\hat{f}(\infty,p)=0, \hat{g}(\infty,p)=0, \hat{\theta}(\infty,p)=0.\end{aligned} \tag{36}$$

3.2 mth order deformation problems

The corresponding problem statements are

$$\mathcal{L}_f\left[j_m(\xi)-\chi_m j_{m-1}(\xi)\right]=\hbar_j\mathcal{R}_{j,m}(\xi), \tag{37}$$

$$\mathcal{L}_f\left[f_m(\xi)-\chi_m f_{m-1}(\xi)\right]=\hbar_f\mathcal{R}_{f,m}(\xi), \tag{38}$$

$$\mathcal{L}_g\left[g_m(\xi)-\chi_m g_{m-1}(\xi)\right]=\hbar_g\mathcal{R}_{g,m}(\xi), \tag{39}$$

$$\mathcal{L}_\theta\left[\theta_m(\xi)-\chi_m\theta_{m-1}(\xi)\right]=\hbar_\theta\mathcal{R}_{\theta,m}(\xi), \tag{40}$$

$$\mathcal{R}_{j,m}(\xi)=j'_{m-1}+2f_{m-1}+m(\xi+\alpha)\epsilon f'_{m-1}, \tag{41}$$

$$\mathcal{R}_{f,m}(\xi) = \mathrm{Re}^{\frac{1-n}{1+n}}(1+r^*)^{2m} f''_{m-1} + \beta \mathrm{Re}^{\frac{1-n}{1+n}}(1+r^*)^{2m} \sum_{k=0}^{m-1} \Big[2f_{m-1-k}f''_k + 4m\epsilon f_{m-1-k}f''_k + 2m\eta\epsilon f_{m-1-k}f'''_k - 2j_{m-1-k}f'''_k + f'_{m-1-k}f'_k + \epsilon f'_{m-1-k}f'_k + m\epsilon\eta f'_{m-1-k}f''_k - j'_{m-1-k}f''_k\Big] + \big(1+\lambda_1\big) \sum_{k=0}^{m-1}\Big[-f'_{m-1-k}f'_k + g'_{m-1-k}g'_k - j_{m-1-k}f'_k\Big] - m(\xi+\alpha)\big(1+\lambda_1\big)\epsilon \sum_{k=0}^{m-1}\Big[f_{m-1-k}f'_k\Big], \tag{42}$$

$$\mathcal{R}_{g,m}(\xi) = \mathrm{Re}^{\frac{1-n}{1+n}}(1+r^*)^{2m} g''_{m-1} + \beta \mathrm{Re}^{\frac{1-n}{1+n}}(1+r^*)^{2m} \sum_{k=0}^{m-1} \Big[2f_{m-1-k}g''_k + 4m\epsilon f_{m-1-k}g''_k + 2m\eta\epsilon f_{m-1-k}g'''_k - 2j_{m-1-k}g'''_k + f'_{m-1-k}g'_k + m\epsilon f'_{m-1-k}g'_k + m\epsilon\eta f'_{m-1-k}g''_k - j'_{m-1-k}g''_k\Big] + \big(1+\lambda_1\big) + \sum_{k=0}^{m-1}\Big[-2f_{m-1-k}g_k + j_{m-1-k}g'_k\Big] - m(\xi+\alpha)\epsilon \sum_{k=0}^{m-1}\Big[f_{m-1-k}g'_k\Big], \tag{43}$$

$$\mathcal{R}_{\theta,m}(\xi) = \frac{1}{\mathrm{Pr}}\mathrm{Re}^{\frac{1-n}{1+n}}(1+r^*)^{2m}\theta''_{m-1} - m(\xi+\alpha)\epsilon\sum_{k=0}^{m-1}\theta'_{m-1-k}f_k - \sum_{k=0}^{m-1}\theta'_{m-1-k}j_k - \gamma\Bigg(\theta''_{m-1-l}\sum_{h=0}^{l}[m(m-1)(\xi+\alpha)\epsilon^2 f_{l-h}f_h + j_{l-h}j_h] + \theta'_{m-1-l}\sum_{h=0}^{l}[m\epsilon j_{l-h}f_h + m(\xi+\alpha)\epsilon f_{l-h}f_h m^2(\xi+\alpha)\epsilon^2 f_{l-h}f'_h + m(\xi+\alpha)\epsilon j_{l-h}f'_h + m(\xi+\alpha)r^* f_{l-h}j'_h] + \theta_{m-1-l}\sum_{h=0}^{l} j_{l-h}j'_h\Bigg), \tag{44}$$

$$f_m(0) = f_m(\infty) = g_m(0) = g_m(\infty) = j_m(0) = \theta_m(0) = \theta_m(\infty) = 0, \tag{45}$$

$$\chi_m = \begin{cases} 0, & m \le 1 \\ 1, & m > 1 \end{cases}. \tag{46}$$

The general solutions $(j_m, f_m, g_m, \theta_m)$ with particular values $(j^*_m, f^*_m, g^*_m, \theta^*_m)$ are

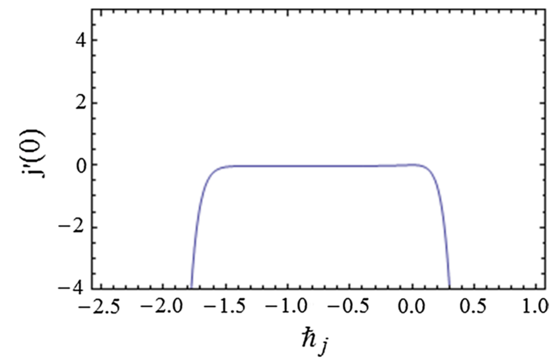

Fig. 2 $\hbar$-curve for $j'(0)$ when $m = 1.0$, $\alpha = 0.15$, $\mathrm{Re} = 1.0$, $n = 1.1$, $\epsilon = 0.4$, $r^* = 0.2$, $\mathrm{Pr} = 1.5$, $\gamma = 0.6$, $\lambda_1 = 0.5$ and $\beta = 0.25$

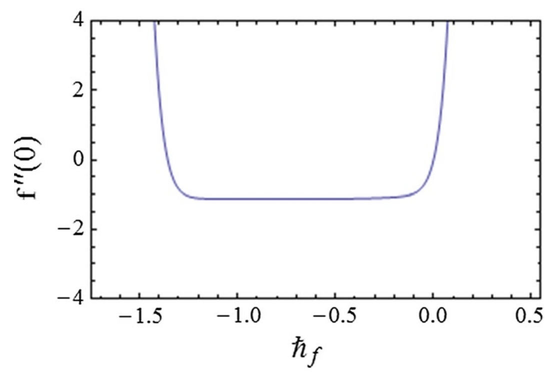

Fig. 3 $\hbar$-curve for $f''(0)$ when $m = 1.0$, $\alpha = 0.15$, $\mathrm{Re} = 1.0$, $n = 1.1$, $\epsilon = 0.4$, $r^* = 0.2$, $\mathrm{Pr} = 1.5$, $\gamma = 0.6$ $\lambda_1 = 0.5$ and $\beta = 0.25$

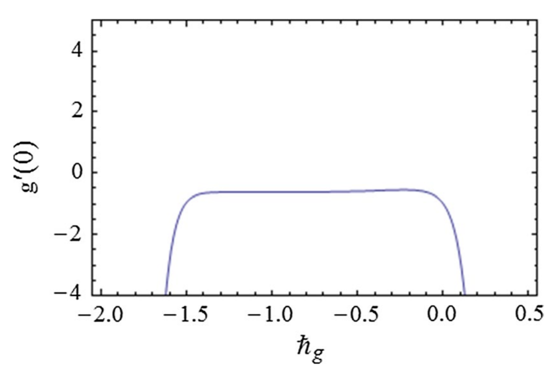

Fig. 4 $\hbar$-curve for $g'(0)$ when $m = 1.0$, $\alpha = 0.15$, $\mathrm{Re} = 1.0$, $n = 1.1$, $\epsilon = 0.4$, $r^* = 0.2$, $\mathrm{Pr} = 1.5$, $\gamma = 0.6$ $\lambda_1 = 0.5$ and $\beta = 0.25$

$$j_m(\xi) = j^*_m(\xi) + c_1, \tag{47}$$

$$f_m(\xi) = f^*_m(\xi) + c_2 e^{-\xi} + c_3 e^{\xi}, \tag{48}$$

$$g_m(\xi) = g^*_m(\xi) + c_4 e^{-\xi} + c_5 e^{\xi}, \tag{49}$$

$$\theta_m(\xi) = \theta^*_m(\xi) + c_6 e^{-\xi} + c_7 e^{\xi}. \tag{50}$$

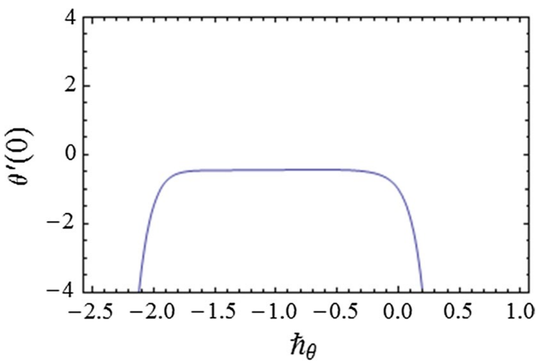

Fig. 5 $\hbar$-curve for $\theta'(0)$ when $m = 1.0$, $\alpha = 0.15$, $\mathrm{Re} = 1.0$, $n = 1.1$, $\epsilon = 0.4$, $r^* = 0.2$, $\mathrm{Pr} = 1.5$, $\gamma = 0.6$ $\lambda_1 = 0.5$ and $\beta = 0.25$

Table 1 Convergence of HAM solutions for different order of approximations when $m = 1.0$, $\alpha = 0.15$, $\mathrm{Re} = 1.0$, $n = 1.1$, $\epsilon = 0.4$, $r^* = 0.2$, $\mathrm{Pr} = 1.5$, $\gamma = 0.6$, $\lambda_1 = 0.5$ and $\beta = 0.25$

Order of approximations	$-j'(0)$	$-f''(0)$	$-g'(0)$	$-\theta'(0)$
1	0	1.43	0.520	0.776
2	0.0321	0.901	0.544	0.650
5	0.0304	1.12	0.558	0.509
11	0.0327	1.13	0.619	0.462
13	0.0324	1.13	0.621	0.460
16	0.0321	1.12	0.621	0.460
20	0.0321	1.12	0.621	0.460
25	0.0321	1.12	0.621	0.460
30	0.0321	1.12	0.621	0.460
40	0.0321	1.12	0.621	0.460
50	0.0321	1.12	0.621	0.460

Table 2 Comparison of the present solutions with the results in Refs. [10, 18] for $n = Pr = 1$, $m = \alpha = \gamma = \lambda_1 = \beta = 0$

Author	$f'(0)$	$-g'(0)$	$-\theta'(0)$
Present	0.51021	0.61592	0.39631
Ming et al. [10]	0.51021	0.61591	0.39632
Xun et al. [18]	0.510231	0.615921	0.396271

4 Analysis

4.1 Convergence of derived series solutions

The region of convergence of series solutions can be adjusted with the help of auxiliary parameters $\hbar_j, \hbar_f, \hbar_g$ and $\hbar_\theta$. For this reason, we have plotted $\hbar$-curves (see Figs. 2, 3, 4 and 5) of $j'(0)$, $f''(0)$, $g'(0)$ and $\theta'(0)$. Appropriate ranges of auxiliary parameters $\hbar_j, \hbar_f, \hbar_g$ and $\hbar_\theta$ are $[-1.49, -0.3]$, $[-1.15, -0.4]$, $[-1.3, -0.65]$ and $[-0.9, -0.4]$, respectively.

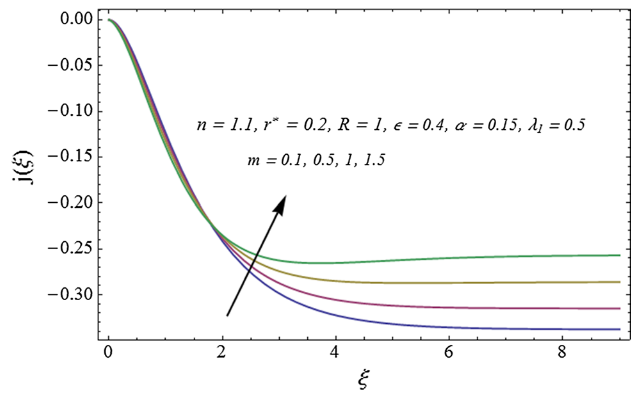

Fig. 6 Impact of m on axial velocity

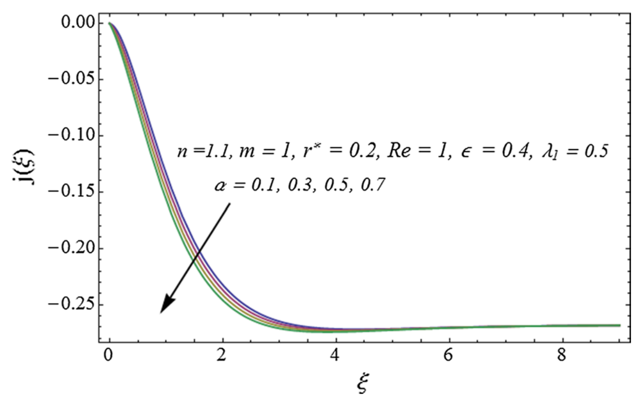

Fig. 7 Impact of α on axial velocity

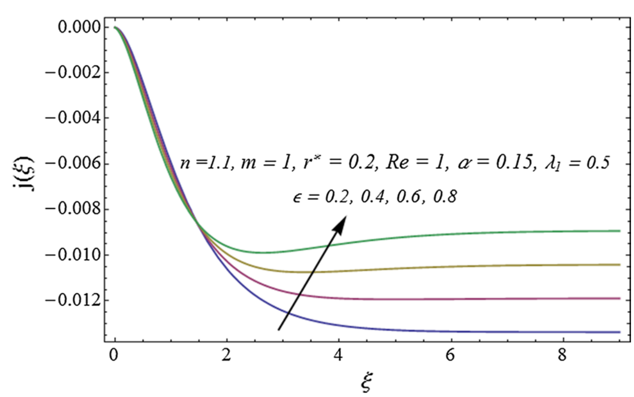

Fig. 8 Impact of ϵ on axial velocity

Convergence of HAM solutions for different order of approximations is given in Table 1. Table 2 is constructed to compare our results with the previous published Refs. [10, 18], and the results are found in excellent agreement

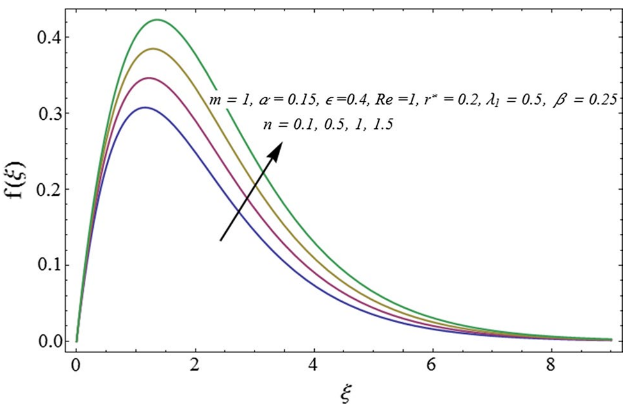

Fig. 9 Impact of n on radial velocity

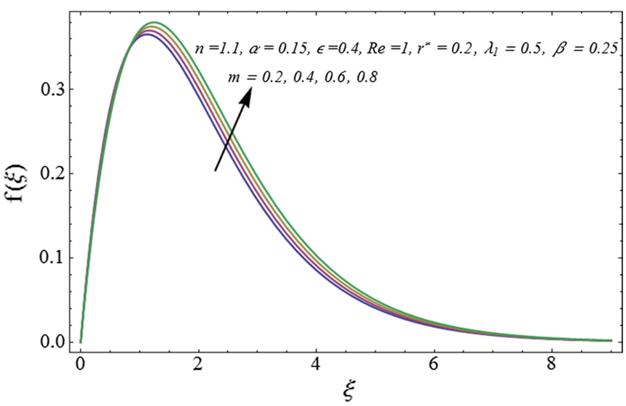

Fig. 10 Impact of m on radial velocity

4.2 Discussion

4.2.1 Axial velocity profile

Figure 6 analyzes the impact of disk thickness index m on axial velocity profile. Here, magnitude of velocity field decreases for rising values of m . Influence of thickness coefficient of disk α on axial velocity profile is shown in Fig. 7. Here, magnitude of velocity profile increases for increasing values of α. Figure 8 is plotted to show the impact of ϵ on axial velocity profile. Here, axial velocity decays for higher values of ϵ.

4.2.2 Radial velocity profile

Influence of power law exponent of fluid n on radial velocity is sketched in Fig. 9. Radial velocity increases for ascending values of n. Thickness of disk decreases for increasing values of n which enhances the fluid velocity. Figure 10 demonstrates the impact of thickness index parameter m on radial velocity field. Here, radial velocity profile enhances for ascending values of m. Variations of α and ϵ on radial velocity are plotted in Figs. 11 and 12.

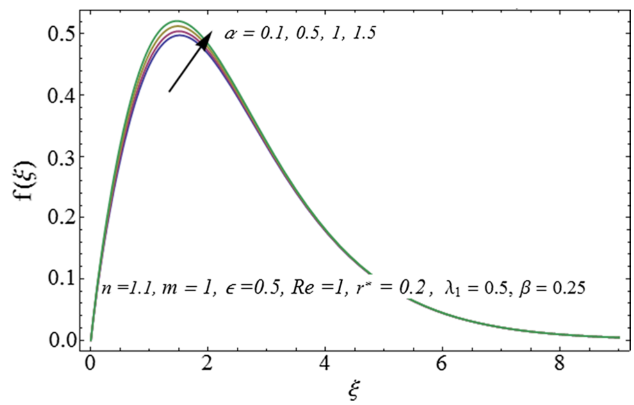

Fig. 11 Impact of α on radial velocity

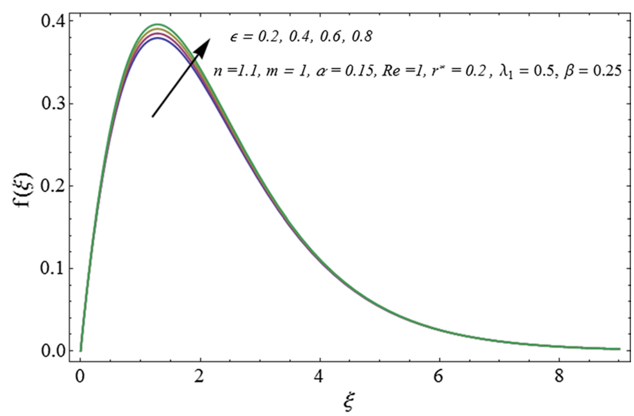

Fig. 12 Impact of ϵ on radial velocity

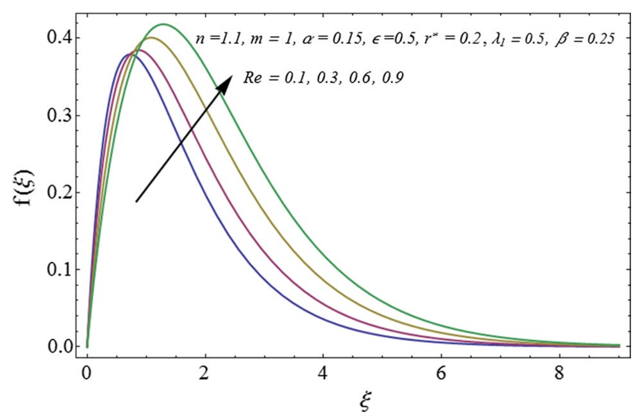

Fig. 13 Impact of Re on radial velocity

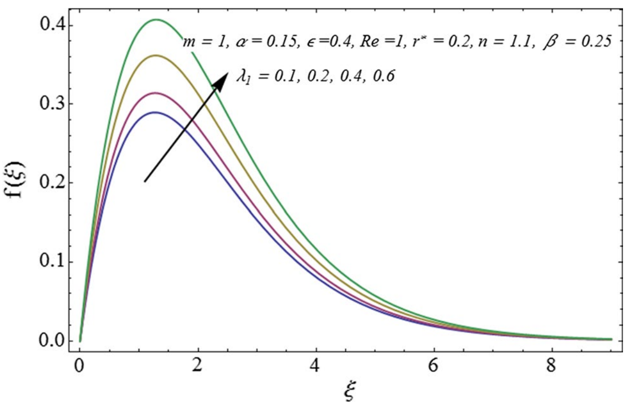

Fig. 14 Impact of λ_1 on radial velocity

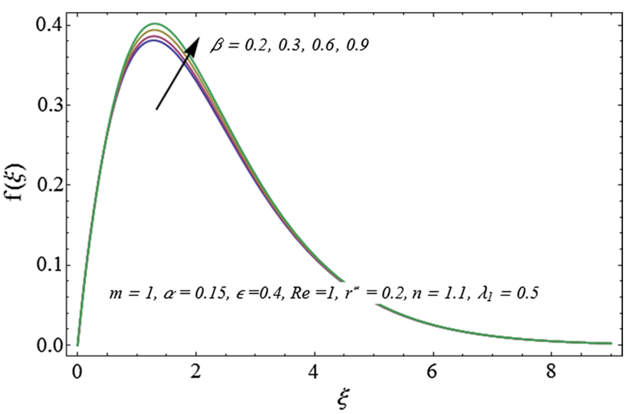

Fig. 15 Impact of β on radial velocity

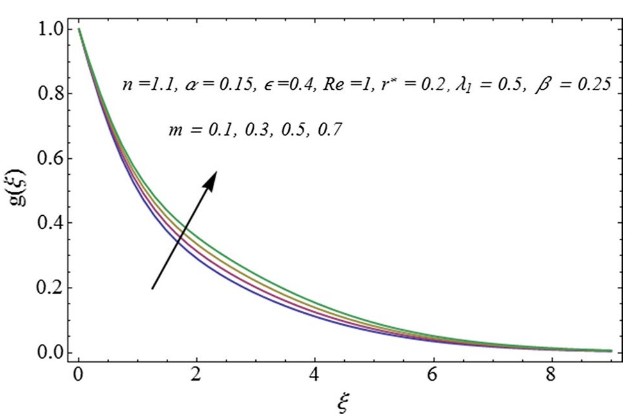

Fig. 16 Impact of m on tangential velocity

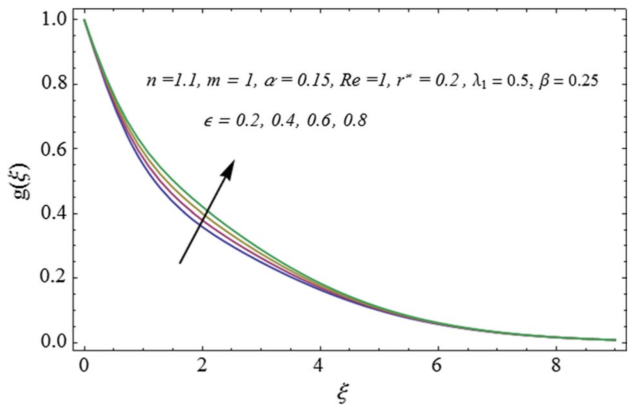

Fig. 17 Impact of ϵ on tangential velocity

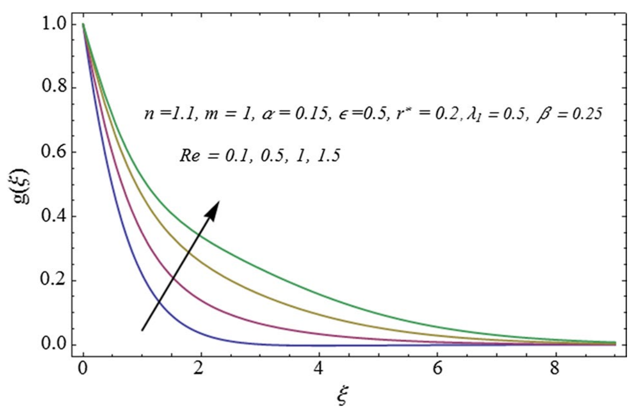

Fig. 18 Impact of Re on tangential velocity

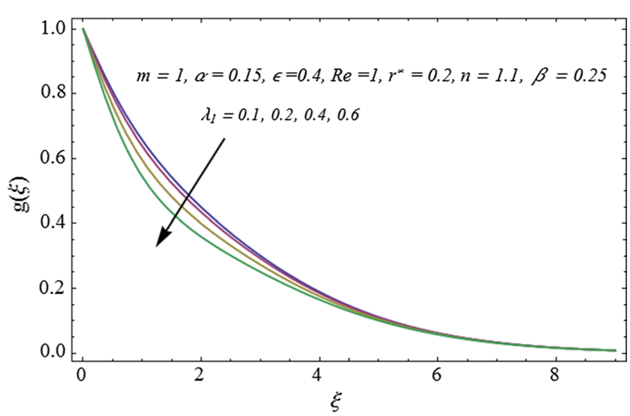

Fig. 19 Impact of λ_1 on tangential velocity

It is seen that velocity rises for increasing values of α and ϵ. Figure 13 depicts the behavior of Re on radial velocity profile. Velocity profile shows increasing behavior of Re. It is due to the fact that viscosity decays for larger values of Re which enhances the fluid velocity. Figure 14 analyzes the increasing behavior of λ_1 on radial velocity profile. It is observed that boundary layer thickness rises when λ_1 is enhanced. It is seen from Fig. 15 that radial velocity has direct relation with Deborah number β. Boundary layer thickness and velocity profile enhance

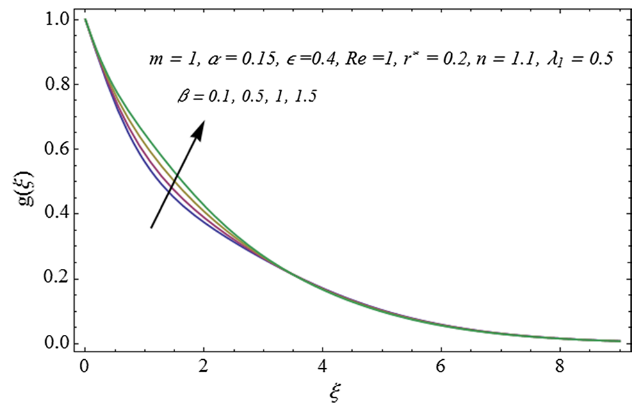

Fig. 20 Impact of β on tangential velocity

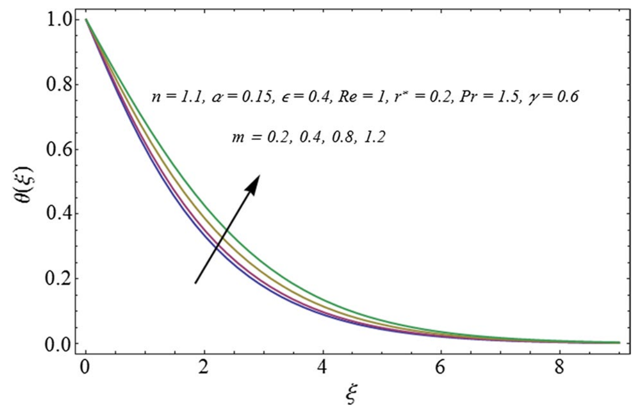

Fig. 22 Impact of m on $\theta(\xi)$

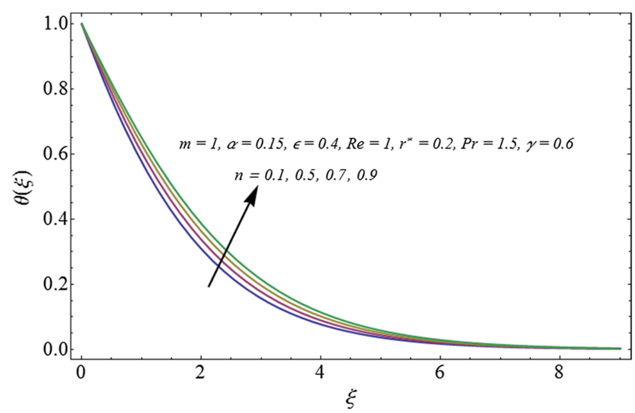

Fig. 21 Impact of n on $\theta(\xi)$

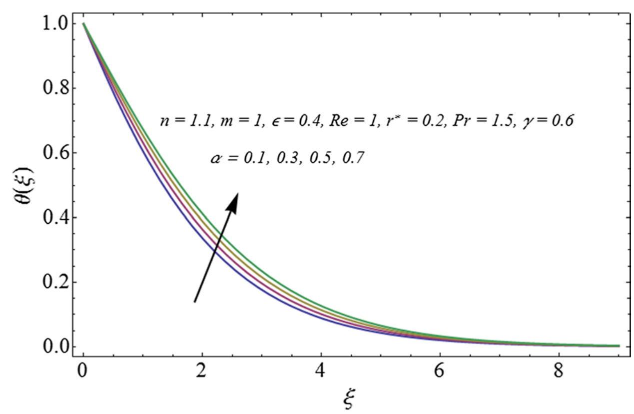

Fig. 23 Impact of α on $\theta(\xi)$

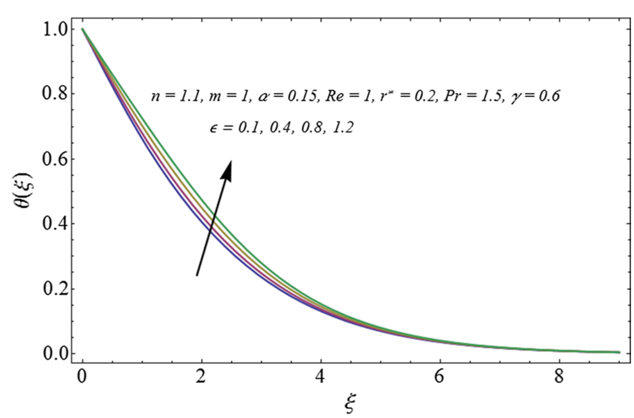

Fig. 24 Impact of ϵ on $\theta(\xi)$

for larger β. As expected, increasing values of retardation time enhance the elasticity.

4.2.3 Tangential velocity profile

Figures 16 and 17 show distribution of tangential velocity profile $g(\xi)$ for larger values of thickness index parameter m and constant ϵ. It is observed that tangential velocity enhances for ascending values of m and constant ϵ. Figure 18 is plotted to demonstrate the impact of Re on tangential velocity. Here, tangential velocity field rises when Re is enlarged. Higher values of Re decrease the viscosity, and thus, fluid velocity enhances. Variation in tangential velocity for larger values of λ_1 is characterized in Fig. 19. We observed that tangential velocity declines for increasing values of λ_1. Since relaxation time increases corresponding to larger λ_1,particles need more time to come back to equilibrium system from perturbed system. As a consequence fluid velocity decreases. Increment in tangential velocity profile for increasing values of Deborah number β is displayed in Fig. 20. Tangential velocity increases for rising values of β. Fluid velocity and boundary layer thickness are enhanced for increasing values of β.

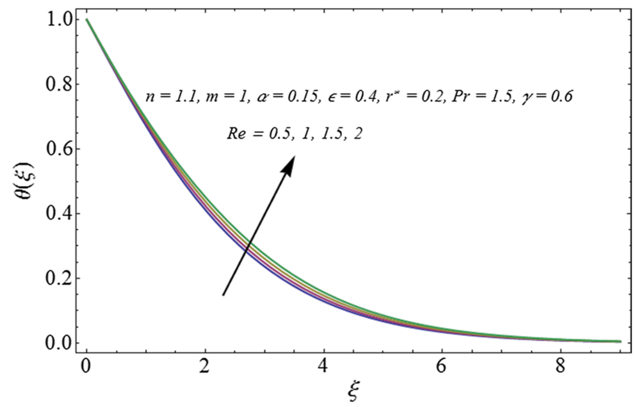

Fig. 25 Impact of Re on $\theta(\xi)$

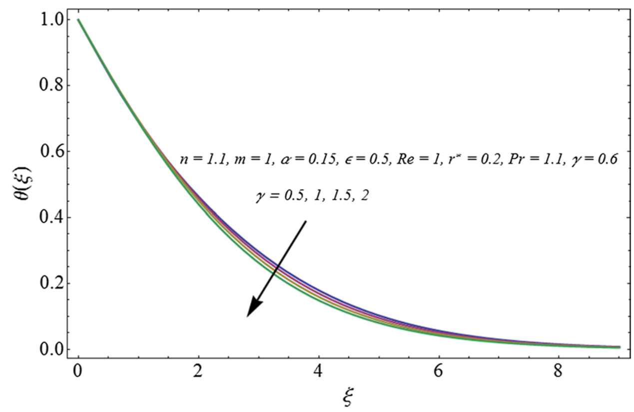

Fig. 28 Impact of γ on $\theta(\xi)$

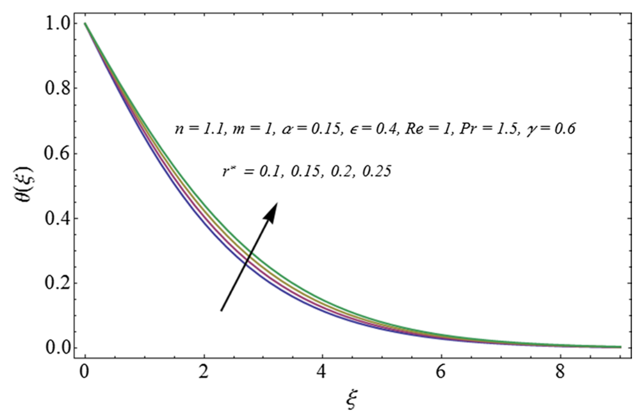

Fig. 26 Impact of r^* on $\theta(\xi)$

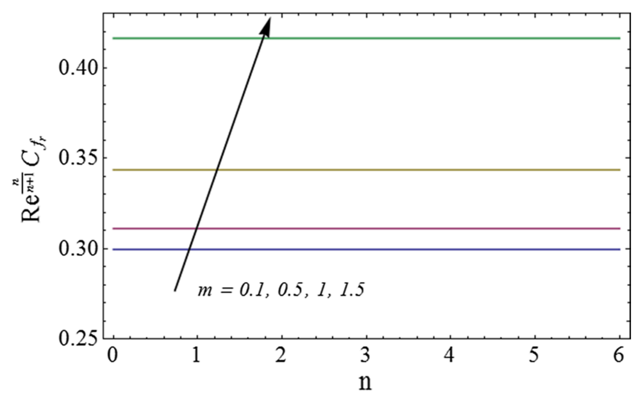

Fig. 29 Behavior of m on $\mathrm{Re}^{\frac{n}{n+1}} C_{f_r}$

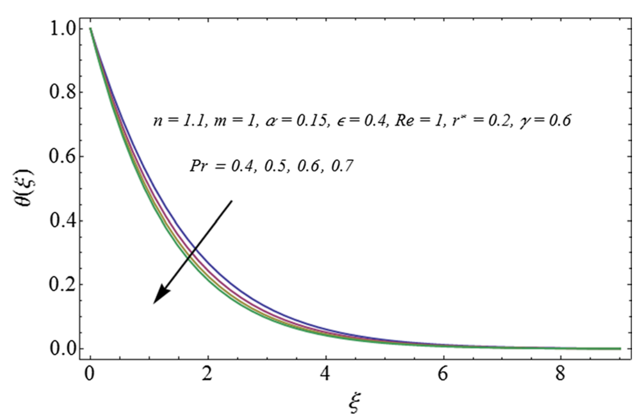

Fig. 27 Impact of Pr on $\theta(\xi)$

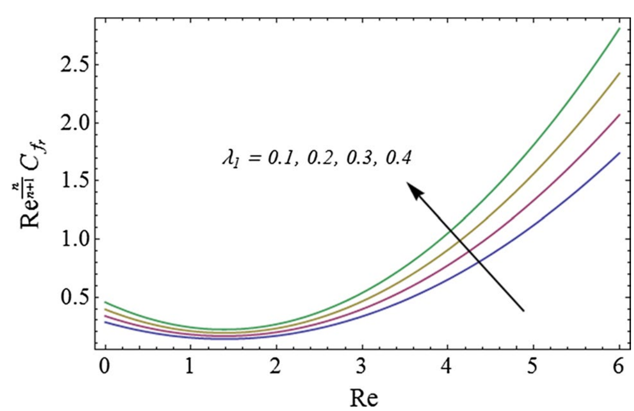

Fig. 30 Behavior of λ_1 on $\mathrm{Re}^{\frac{n}{n+1}} C_{f_r}$

4.2.4 Dimensionless temperature profile

Figure 21 discloses the behavior of power law exponent n on temperature field. Temperature of fluid enhances for larger values of n. Figure 22 reveals the variation of index parameter m on temperature. Here, increase in m enlarges temperature distribution. Influence of thickness coefficient of disk α on temperature is indicated in Fig. 23. Temperature distribution rises corresponding to higher values of α. Figure 24 illustrates the variation of ϵ on

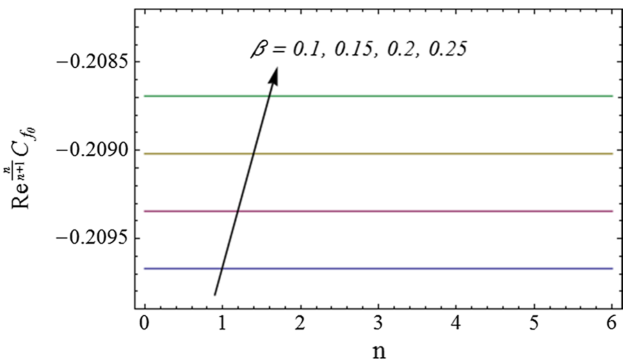

Fig. 31 Behavior of β on $\mathrm{Re}^{\frac{n}{n+1}} C_{f_\theta}$

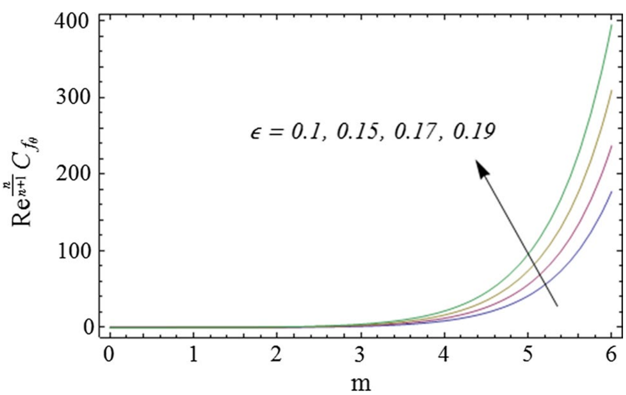

Fig. 32 Behavior of ϵ on $\mathrm{Re}^{\frac{n}{n+1}} C_{f_\theta}$

temperature field. It is seen that temperature is increasing function of ϵ. Figures 25 and 26 analyze the increasing behavior of Re and r^* on temperature distribution. Impact of Prandtl number Pr on temperature distribution is presented in Fig. 27. Here, temperature profile reduces when Pr is enhanced. Prandtl number is ratio of momentum diffusivity to thermal diffusivity. Larger values of Prandtl number reduce the thermal diffusivity, and so, temperature distribution decreases. Figure 28 portrays the influence of thermal relaxation parameter on temperature profile. For higher values of γ the temperature and thermal layer thickness reduced. In fact, particles require more time to transfer heat which decreases the temperature distribution.

4.2.5 Radial skin friction coefficient

Behavior of thickness index parameter m (via n) on radial skin friction coefficient is examined in Fig. 29. Surface drag force enhances for larger m. Figure 30 illustrates the impact of λ_1 on radial skin friction coefficient against Re. Here, surface drag force rises for ascending values of λ_1.

4.2.6 Tangential skin friction coefficient

Figures 31 and 32 reveal the impact of β and ϵ on tangential skin friction coefficient. Here, we noticed that magnitude of skin surface drag force decreases for ascending values of β and ϵ.

5 Concluding remarks

Axisymmetric flow of Jeffrey fluid by a rotating disk with variable thicked surface is studied. Heat transfer is discussed through Cattaneo–Christov heat flux model. HAM is used to obtain analytical solutions. It is observed that for larger values of the ratio of relaxation to retardation times λ_1, the velocity along radial direction increases, while it reduces along tangential direction. Radial and tangential velocities have direct relation with Deborah number β. An increase in retardation time enhances elasticity. Since elasticity and viscosity effects are inversely proportional to each other, decrease in viscosity enhances the fluid velocity. For larger thermal relaxation time parameter, particles require more time to transfer heat which decreases the temperature distribution. Higher thickness index of disk m implies an enhancement in the skin friction coefficient in redial direction.

References

1. Narayana PVS, Babu DH (2016) Numerical study of MHD heat and mass transfer of a Jeffrey fluid over a stretching sheet with chemical reaction and thermal radiation. J Taiwan Inst Chem Eng 59:18–25
2. Turkyilmazoglu M (2016) Magnetic field and slip effects on the flow and heat transfer of stagnation point Jeffrey fluid over deformable surfaces. Zeitschrift für Naturforschung A 71:549–556
3. Abbasi FM, Shehzad SA, Hayat T, Alhuthali MS (2016) Mixed convection flow of jeffrey nanofluid with thermal radiation and double stratification. J Hydrodyn 28:840–849
4. Shehzad SA, Abdullah Z, Alsaedi A, Abbasi FM, Hayat T (2016) Thermally radiative three-dimensional flow of Jeffrey nanofluid with internal heat generation and magnetic field. J Magn Magn Mater 397:108–114
5. Zeeshan A, Majeed A (2016) Heat transfer analysis of Jeffery fluid flow over a stretching sheet with suction/injection and magnetic dipole effect. Alex Eng J 55:2171–2181
6. Dalir N (2014) Numerical study of entropy generation for forced convection flow and heat transfer of a Jeffrey fluid over a stretching sheet. Alex Eng J 53:769–778
7. Turkyilmazoglu M, Pop I (2013) Exact analytical solutions for the flow and heat transfer near the stagnation point on a stretching/shrinking sheet in a Jeffrey fluid. Int J Heat Mass Transf 57:82–88
8. Hayat T, Awais M, Obaidat S (2012) Three-dimensional flow of a Jeffery fluid over a linearly stretching sheet. Commun Nonlinear Sci Numer Simul 17:699–707
9. Karman TV (1921) Uber laminare and turbulente Reibung. Z Angew Math Mech 1:1233–1252

10. Ming CY, Zheng LC, Zhang XX (2011) Steady flow and heat transfer of the power law fluid over a rotating disk. Int Commun Heat Mass 38:280–284
11. Turkyilmazoglu M (2014) Nanofluid flow and heat transfer due to a rotating disk. Comput Fluids 94:139–146
12. Bayat M, Rahimi M, Saleem M, Mohazzab AH, Wudtke I, Talebi H (2014) One-dimensional analysis for magneto-thermo-mechanical response in a functionally graded annular variable-thickness rotating disk. Appl Math Model 38:4625–4639
13. Sheikholeslami M, Hatami M, Ganji DD (2015) Numerical investigation of nanofluid spraying on an inclined rotating disk for cooling process. J Mol Liq 211:577–583
14. Hayat T, Nawaz M, Awais M, Obaidat S (2012) Axisymmetric magnetohydrodynamic flow of Jeffrey fluid over a rotating disk. Int J Numer Methods Fluids 70:764–774
15. Turkyilmazoglu M (2016) Flow and heat simultaneously induced by two stretchable rotating disks. Phys Fluids 28:043601
16. Hayat T, Qayyum S, Imtiaz M, Alsaedi A (2016) Three-dimensional rotating flow of Jeffrey fluid for Cattaneo–Christov heat flux model. AIP Adv 6:025012
17. Saidi MH, Tamim H (2016) Heat transfer and pressure drop characteristics of nanofluid in unsteady squeezing flow between rotating porous disks considering the effects of thermophoresis and Brownian motion. Adv Powder Technol 27:564–574
18. Xun S, Zhao J, Zheng L, Chen X, Zhang X (2016) Flow and heat transfer of Ostwald-de Waele fluid over a variable thickness rotating disk with index decreasing. Int J Heat Mass Transf 103:1214–1224
19. Fourier JBJ (1822) Theorie Analytique De La Chaleur. Académie des Sciences, Paris
20. Cattaneo C (1948) Sulla conduzione del calore. Atti Semin Mat Fis Univ Modena Reggio Emilia 3:83–101
21. Christov CI (2009) On frame indifferent formulation of the Maxwell–Cattaneo model of finite speed heat conduction. Mech Res Commun 36:481–486
22. Tibullo V, Zampoli V (2011) A uniqueness result for the Cattaneo–Christov heat conduction model applied to incompressible fluids. Mech Res Commun 38:77–79
23. Han S, Zheng L, Li C, Zhang X (2014) Coupled flow and heat transfer in viscoelastic fluid with Cattaneo–Christov heat flux model. Appl Math Lett 38:87–93
24. Hayat T, Imtiaz M, Alsaedi A, Almezal S (2016) On Cattaneo–Christov heat flux in MHD flow of Oldroyd-B fluid with homogeneous–heterogeneous reactions. J Magn Magn Mater 401:296–303
25. Sui J, Zheng L, Zhang X (2016) Boundary layer heat and mass transfer with Cattaneo–Christov double-diffusion in upper-convected Maxwell nanofluid past a stretching sheet with slip velocity. Int J Therm Sci 104:461–468
26. Mustafa M (2015) Cattaneo–Christov heat flux model for rotating flow and heat transfer of upper-convected Maxwell fluid. AIP Adv 5:047109
27. Li J, Zheng L, Liu L (2016) MHD viscoelastic flow and heat transfer over a vertical stretching sheet with Cattaneo–Christov heat flux effects. J Mol Liq 221:19–25
28. Abbasbandy S, Shivanian E (2011) Predictor homotopy analysis method and its application to some nonlinear problems. Commun Nonlinear Sci Numer Simul 16:2456–2468
29. Ganji DD, Abbasi M, Rahimi J, Gholami M, Rahimipetroudi I (2014) On the MHD squeeze flow between two parallel disks with suction and or injection via HAM and HPM. Front Mech Eng 9:270–280
30. Farooq U, Zhao YL, Hayat T, Alsaedi A, Liao SJ (2015) Application of the HAM-based mathematica package BVPh 2.0 on MHD Falkner–Skan flow of nanofluid. Comput Fluids 111:69–75
31. Daniel YS, Daniel SK (2015) Effects of buoyancy and thermal radiation on MHD flow over a stretching porous sheet using homotopy analysis method. Alex Eng J 54:705–712
32. Ellahi R, Hassan M, Zeeshan A (2015) Shape effects of nanosize particles in Cu–H_2O nanofluid on entropy generation. Int J Heat Mass Transf 81:449–456
33. Sui J, Zheng L, Zhang X, Chen G (2015) Mixed convection heat transfer in power law fluids over a moving conveyor along an inclined plate. Int J Heat Mass Transf 85:1023–1033
34. Hayat T, Khan MI, Farooq M, Alsaedi A, Waqas M, Yasmeen T (2016) Impact of Cattaneo–Christov heat flux model in flow of variable thermal conductivity fluid over a variable thicked surface. Int J Heat Mass Transf 99:702–710
35. Turkyilmazoglu M (2018) Convergence accelerating in the homotopy analysis method: a new approach. Adv Appl Math Mech 10:1–24